Draft version November 29, 2025
Typeset using LaTeX **twocolumn** style in AASTeX631

Axion Signatures of M87 with Polarimetry of Relativistic Jets

Dashon Jones,[1,2,3] Richard Anantua,[2,3,4] Razieh Emami,[3] and Nate Lujan[4]

[1]*Physics Astronomy Department, Rice University, Houston, Texas 77005-1827, USA*
[2]*Black Hole Initiative at Harvard University, 20 Garden Street, Cambridge MA 02138, USA*
[3]*Harvard-Smithsonian Center for Astrophysics, 60 Garden Street, Cambridge MA 02138, USA*
[4]*Physics and Astroomy Department, University of Texas at San Antonio, 1 UTSA Circle, San Antonio, TX 78249*

(Dated: July 2025)

ABSTRACT

Axions, or axion-like particles(ALPs), are a prime dark matter candidate motivated by the Strong CP problem. A linearly polarized photon propagating in an ALP field can have induced periodic oscillations about the electron vector position angle(EVPA). Thee changes to the polarization have increased the interest of searching for axion signatures in astrophysical environments. A novel and unique of searching polarimetric measurements for axion signatures has been to use the relatively recent Event Horizon Telescope(EHT) array which recently produced images of the magnetic fields lines around the supermassive black holes M87 and Sgr A*. However, much of the previous literature on this study focuses on radiation coming from the accretion disk rather than a relativistic jet. In this study, we investigate the effects of an axion cloud around M87 on the Stokes maps of relativistic jets using a stationary, axisymmetric, self-similar model for the jet. We focus on the case of a soliton core forming in the galactic center with and axion-photon coupling constant of $g_{a\gamma}$ followed by discussions of the superradiance case to be done in the near future. We show that with a strong enough coupling, we can see notable changes in the polarization maps of the jets with the maximal angle change increasing with increasing mass.

Keywords: General Relativity — Black Holes — Dark Matter — Axions — Polarimetry

1. INTRODUCTION

The Event Horizon Telescope (EHT), which ushered in the age of direct imaging of supermassive black holes with the sources M87* in 2019 and Sgr A* in 2022 (Event Horizon Telescope Collaboration et al. 2019, 2022), opens a new era for probing physics in the extreme environment of a supermassive black hole(SMBH). This level of unprecedented resolution has opened many avenues for exploring fundamental physics with the EHT (Ayzenberg et al. 2023). While this allows to investigate tests of general relativity, accretion disk physics, and extreme electrodynamics in the strong gravity regime, it offers new avenues to study Beyond Standard Model(BSM) physics around compact objects. More recently, the EHT has been able to resolve the polarized images of both Sgr A* (Event Horizon Telescope Collaboration et al. 2024) and M87 (Collaboration et al. 2021), which has raised the interest of researchers looking to study BSM phenomenology around black holes. With the advantages of Very Long Baseline Inteferomtry(VLBI)and polarimetric measurements of the radiation, the EHT serves as a unique probe to constrain the existence of axion-like particles(ALPs) in astrophysical environments. Many of these searches typically attempt to search for axion effects on the electromagnetic sector (Tobar et al. 2019).

The axion is a hypothetical BSM particle motivated by being a solution to the strong CP problem (Weinberg 1978) in quantum chromodynamics(QCD). Quantum field theory predicts that the QCD Largangian violates CP symmetry, yet, QCD seems to preserve it. Beyond QCD, ALPs generically appear in fundamental theories and string theories, serving as a viable dark matter candidate. There have been many proposed ways to search for axion signatures including nuclear magnetic resonance (Arvanitaki & Geraci 2014), neutron stars (Noordhuis et al. 2024), and gravitational wave signatures (Gorghetto et al. 2021).

Ultralight axions may be treated as a classical wave due to their exceptionally high occupation number (Hui 2021). An analytic model of a DM halo formed in this regime can be described by a Schrodinger-Poisson system (Manita et al. 2024) and a soliton core can form in the galactic center due to the balance between gravitational interactions and the quantum pressure (Mocz et al. 2023). The spatial mass and density distribution of such halos is often described by a Navarro–Frenk–White (NFW) profile which is used in many cosmological simulations of cold dark matter(CDM) in galaxies, such as effects on structure formation (Mina et al. 2022).

When the Compton wavelength of the axion field is comparable to the size of the BH, the axion cloud can be excited due to rotational superradaince (Teukolsky 1972). This is a generalized version of the Penrose process (Lasota et al. 2014) which typically focuses on a classical particle (Penrose & Floyd 1971). Historically, searches for BH superradiance signatures have focused on gravitational wave signals from bosenova (Arvanitaki & Dubovsky 2011). More recently, it has been proposed that the high spatial resolution and polarimetric measurements of the EHT can be used to probe axion cloud around an SMBH (Chen et al. 2020). This is because a photon passing through an axion cloud can have axion-induced time oscillations of the Electriv Vector Position Angle(EVPA), similar to the classical Faraday rotation effect.

In this paper, we propose searches for axions around M87 using polarimetric measurements of relativistic jets. The analysis focuses on how ALPs could theoretically affect the polarization maps of jets. This paper is structured as follows. In Section 2, we present the configuration for an ambient DM cloud that forms a soliton core in the galactic center of M87. This is well motivated and is the simplest to work with. In Section 3, we briefly review the superradiance mechanism and briefly discuss its use in our polarization analysis. Section 4 reviews the jet model found in (Anantua et al. 2020) followed by Section 5 which discusses the interaction between axions and the Standard Model, particularly electromagnetism. In Section 6 we present methods used to study the polarization maps with and the axion-induced maps generated for the soliton core model. We summarize in Section 7 and present further analyses to be undertaken in the near future.

2. COHERENT ALP FIELD

A linearly polarized photon traveling through an ALP field can have periodic rotation of the Electron Vector Position Angle(EVPA). The relevant Lagrangian for an ALP field coupled to electromagnetism is the following:

$$\mathcal{L} = -\frac{1}{4}F_{\mu\nu}F^{\mu\nu} + \frac{1}{2}\partial_\mu a\,\partial^\mu a - \frac{1}{2}m_a^2\,a^2 - \frac{g_{a\gamma}}{4}\,a\,F_{\mu\nu}\tilde{F}^{\mu\nu} \tag{1}$$

were $F_{\mu\nu} = \partial_\mu A_\nu - \partial_\nu A_\mu$ and $\tilde{F}^{\mu\nu}$ is the dual. The equation of motion for the ALP field arising from this is,

$$\Box a + m_a^2 = g_{a\gamma}\boldsymbol{E}\cdot\boldsymbol{B} \tag{2}$$

By assuming that the source term is negligible compared to $m_a^2 a$, we can ignore the back-reaction term. The solution then becomes a coherently oscillating ALP field,

$$a(t,\vec{x}) \approx a_0 sin[m_a t - \delta(\vec{x})], \quad a_0 = \sqrt{\frac{\rho_{DM}}{m_a^2}} \tag{3}$$

where $\delta(\vec{x})$ is a position-dependent phase. For axion experiments on Earth, the value of this tends to be in the vicinity of $\rho_{DM} \approx 0.4GeV/cm^{-3}$. This value tends to be much larger in many astrophysical systems, including near a Kerr black hole. It is valid to describe such a field as a classical field since axions within this mass range have exceptionally small interparticle separation characterized by the de Brogile wavelength (Hui 2021). For ultralight axion DM, the balance between quantum pressure and galactic interactions can give rise to a soliton core near the galactic center. The radius of the core is directly related to the de Brogile wavelength of the ALP field,

$$r_c = \frac{2\pi}{m_a v} \tag{4}$$

where v is the average velocity of the dark matter within the specified galaxy. Within the solitonic core, the radius is assumed to be coherent and homogenous whereas outside the soliton core, the DM density follows an NFW profile. Simulations from (Murphy et al. 2011) suggest the mean velocity of dark matter in M87 to be around $800\frac{km}{s}$ corresponding to $v \approx 2.66 \times 10^-3c$. We will use this value here. The relationship between mass and core radius can be found in Fig. 1.

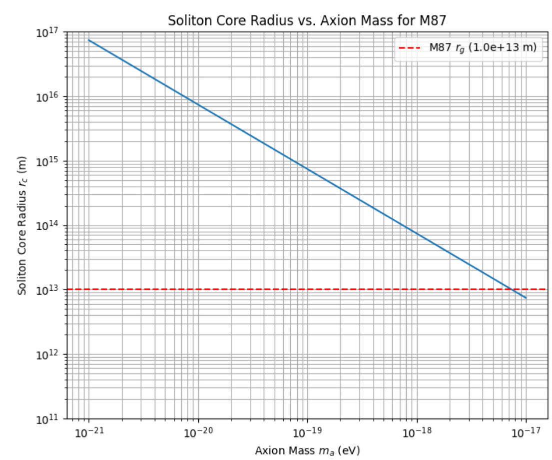

Figure 1: Relationship between axion mass and soliton core radius.

Simulations from (Schive et al. 2014) show that the density profile can be parametrized as follows,

$$\rho_{\rm DM} = \begin{cases} 190 \times \left(\frac{m_a}{10^{-18}\rm eV}\right)^{-2}\left(\frac{r_c}{1\rm pc}\right)^{-4} M_\odot \rm pc^{-3}, & \text{for } r < r_c \\ \frac{\rho_0}{r/R_g(1+r/R_g)^2}, & \text{for } r > r_c \end{cases} \tag{5}$$

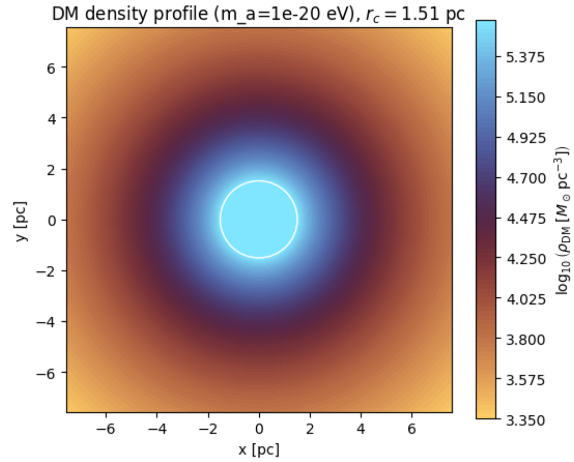

Figure 2: Density profile for dark matter with axion mass of $10^{-20}eV$. White circle highlights the radius of the soliton core of which, density falls off as NFW profile outside this.

Additionally, from the Lagrangian, we get the equation of motion for the electromagnetic field,

$$\ddot{\boldsymbol{A}} - \nabla^2 \boldsymbol{A} = g_{a\gamma}(\dot{a}\nabla \times \boldsymbol{A} + \dot{\boldsymbol{A}} \times \nabla a) \tag{6}$$

which when following in the temporal gauge and Coloumb gauge, can be decomposed into two circular polarization modes, $A^{\pm}$.

$$\boldsymbol{A}(t, \boldsymbol{x}) = \sum_{\pm} \int \frac{d^3k}{(2\pi)^3} A^{\pm}(k) \boldsymbol{e}^{\pm}(\hat{\boldsymbol{k}}) e^{(ik\cdot x - i\omega_{\pm} t)} \tag{2.6}$$

The equations of motion result in two different dispersion relations for each of the two different circularly polarized modes.

$$w_{\pm}^2 - k^2 \mp g_{a\gamma}(\dot{a} + \hat{\boldsymbol{k}} \cdot \nabla a)|k| = 0 \tag{2.7}$$

The misalignment of the ALP field causes spontaneous breaking of the parity symmetry. Such an effect causes birefringence, and for a linearly polarized photon, we will see a change in the position angle in the polarization plane.

$$\Delta\chi = \frac{g_{a\gamma}}{2} \int_{t_{\text{emit}}}^{t_{\text{obs}}} \frac{da}{dt} dt = \frac{g_{a\gamma}}{2} \left[a\left(t_{\text{obs}}, \boldsymbol{x}_{\text{obs}}\right) - a\left(t_{\text{emit}}, \boldsymbol{x}_{\text{emit}}\right)\right] \tag{7}$$

Since the strength of the axion field on Earth is negligible to the strength at the point of emission, we can ignore the observation term.

3. SUPERRADIANCE

In the section, we briefly review the process of an axion cloud forming around an SMBH via rotational superrdiance. This section only serves as an overview of the topic to introduce the basics of how such a process occurs and should not be taken as a replacement for further study. Further theory can be found in (Brito et al. 2020).

We now consider the Lagrangian of an axion field coupled to electromagnetism in curved spacetime. Specifically, we will be working in Boyler-Lindquist(BL) coordinates $x^{\mu} = [t, r, \theta, \phi]$.

$$\mathcal{L} = -\frac{1}{4} F_{\mu\nu} F^{\mu\nu} + \frac{1}{2} \nabla_{\mu} a\, \nabla^{\mu} a - \frac{1}{2} m_a^2\, a^2 - \frac{g_{a\gamma}}{4}\, a\, F_{\mu\nu} \tilde{F}^{\mu\nu} \tag{8}$$

The only difference here is the partial derivatives have been promoted to covariant derivatives. Ignoring the self-interaction term, the KG equation for a scalar field with mass μ is given as,

$$(g^{\alpha\beta} \nabla_{\alpha} \nabla_{\beta} - \mu^2)\Phi = 0 \tag{9}$$

.

The variables in his solution are separable under a Kerr backgroud which allows us to take the following ansatz,

$$a(t, r, \theta, \varphi) = e^{-i\omega t}\, e^{im\varphi}\, S_{\ell m}(\theta)\, R_{\ell m}(r), \qquad m \in \mathbb{Z} \tag{10}$$

where $R_{\ell m}(r)$, is the radial function and $S_{\ell m}(\theta)$ are the spheroidal harmonics. Ingoing boundary conditions are imposed on the outer horizon such that the radial profile falls off exponentially after reaching its peak. The radial function can only be evaluated numerically using Leaver's nomenclature (Dolan 2007), starting with a function of the form,

$$R(r) = (r - r_+)^{-i\sigma} (r - r_-)^{-i\sigma + \chi - 1} e^{qr} \Sigma_{n=0}^{\infty} a_n \left(\frac{r - r_+}{r - r_-}\right)^n \tag{11}$$

where $q = -\sqrt{\mu^2 - \omega^2}$, $\chi = \frac{\mu^2 - 2\omega^2}{q}$, $\sigma = \frac{2r_+(\omega - \omega_c)}{r_+ - r_-}$.

Near the horizon($r \to r_+$), the dominant term in the radial equation gives plane wave solutions,

$$R \sim \begin{cases} e^{-i(\omega - m\Omega_H) r_*} & \text{ingoing } (\ \to H\ ), \\ e^{+i(\omega - m\Omega_H) r_*} & \text{outgoing } (\leftarrow \text{from H}). \end{cases} \tag{12}$$

where $\Omega_h = \frac{a}{2Mr_+}$. Regularity at the horizon requires purely ingoing boundary conditions, so we exclude the outgoing piece.

$$R\big|_{r \to r_+} = \mathcal{T}\, e^{-i(\omega - m\Omega_H) r_*} \tag{13}$$

Here $\mathcal{T}$ is the *transmission amplitude* into the hole. At spatial infinity ($r \to \infty$), for $\omega^2 > \mu^2$ the field is oscillatory:

$$R \sim A_{\rm in}\frac{e^{-ikr_*}}{r} + A_{\rm out}\frac{e^{+ikr_*}}{r}, \quad k \equiv \sqrt{\omega^2 - \mu^2} \quad (14)$$

$A_{\rm in}$ and $A_{\rm out}$ are, respectively, the amplitudes of the incident and reflected waves; $\mathcal{R} \equiv A_{\rm out}/A_{\rm in}$ is the reflection coefficient. We can use the Wronskian to find the relationship between the reflection and transmission coefficients. For any solution to the radial ODE, the quantity,

$$\mathcal{W} \;=\; R^*\,\Delta\,\frac{dR}{dr} - R\,\Delta\,\frac{dR^*}{dr} \quad (15)$$

is constant in r. The Wronskian near the horizon must equal the one at infinity.

$$\mathcal{W}_H = 2(\omega - m\Omega_H)\,|\mathcal{T}|^2 \quad (16)$$

$$\mathcal{W}_\infty = 2k\left(|A_{\rm out}|^2 - |A_{\rm in}|^2\right) = 2k\,|A_{\rm in}|^2\left(|\mathcal{R}|^2 - 1\right) \quad (17)$$

Set $\mathcal{W}_H = \mathcal{W}_\infty$ and we get,

$$k\left(|\mathcal{R}|^2 - 1\right) = (\omega - m\Omega_H)\frac{|\mathcal{T}|^2}{|A_{\rm in}|^2} \quad (18)$$

$$|\mathcal{R}|^2 = 1 - \frac{\omega - m\Omega_H}{k}\frac{|\mathcal{T}|^2}{|A_{\rm in}|^2} \quad (19)$$

Because $k > 0$ and $|\mathcal{T}|^2 > 0$, if we have $\omega - m\Omega_H > 0$, this leads to $|\mathcal{R}|^2 < 1$ which is ordinary absorption. However, if instead, $0 < \omega < m\Omega_H$, then $|\mathcal{R}|^2 > 1$ and we get **amplification**. In other words, we get superradiance and an amplification of the bosonic field. Superradiance takes place efficiently when the Compton wavelength λ_C of the axion field is comparable to the BH size $R_s \sim \lambda_C$, within an order one factor. The axion field forms a bound state with the SMBH and the configuration is often referred to as the "gravitational atom," because of its analogous nature with the hydrogen atom solution.

Typically, the type of field configuration we are working with is tracked via the gravitational fin structure constant, $\alpha = \frac{r_g}{\lambda_C}$, and the quantum numbers n,l and m. Since $\alpha \propto m_a$ and the mass is related to the occupation number of the cloud, we can use the gravitaional fine structure constant as a marker for the radial extent of our cloud.

Higher values of α correspond to lower mass values and a peak closer to the black hole. If one were to consider radiation cases coming from accretion flows, it is favorable to choose values such that the axion field peaks close to the disk and closer the SMBH. For relativistic jets, this depends on the extent of the jet investigated. Generally, the superradiance model depends on the vicinity of the black hole investigated.

Numerical simulations from (Dolan 2007) show that the n=2, l=m=1 state has the highest superradiant rate. Analogously to the hydrogen atom, the shape of the cloud resembles p orbitals with its "dumbbell-like" shape. While other modes may coexist with the 211 state, the 211 state typically dominates near the black hole. Previous analyses of searching for axions with the EHT focuses on this region and often restricted their axion field configuration to just the 211 state. However, higher modes have more spatial extent and become more important when looking at large-scale jet observables. The higher modes may dominate in some of these cases, but calculating the amplitude is more complicated since relativistic effects are strong. Another caveat is that since $a \propto sin(\theta)$ where theta is the polar angle in Kerr spacetime, the axion field is stronger near the equatorial plane where accretion flow is dominant. Since jets tend to align with the spin axis, this could lead to significant surpression of the axion-photon interactions unless the jet has a large opening angle. Additionally, one would have to consider the effects of self-interactions since it effects the evolution of the superradiant instability (Baryakhtar et al. 2021).

4. ANALYTIC RELATIVISTIC JET MODEL

To investigate axion signatures in the polarized emission from M87's relativistic jet, we employ the semi-analytic jet model developed by (Anantua et al. 2020). This model provides a computationally efficient framework for generating synthetic polarimetric observations while capturing the essential physics of magnetically dominated jet flows. The advantage of this approach is twofold: it enables us to explore parameter space systematically without the computational expense of full general relativistic magnetohydrodynamic (GRMHD) simulations, and its self-similar structure allows us to model jet physics across a wide range of spatial scales—from the black hole horizon ($\sim 10M$) to large-scale jet structures ($\sim 10^5 M$), where $M \equiv GM_{\rm BH}/c^2$ is the gravitational radius.

4.1. *Self-similar Stationary Semi-analytic Model*

The jet model is based on force-free regions of relativistic GRMHD simulations and assumes the plasma is stationary ($\partial/\partial t = 0$) and axisymmetric ($\partial/\partial\phi = 0$). These assumptions are well-justified for the time-averaged structure of AGN jets and significantly simplify the analysis while preserving the key electromagnetic properties relevant for polarization studies.

The model employs cylindrical coordinates (s, ϕ, z), where s is the cylindrical radius and z is the height along the jet axis. The self-similarity of the flow is characterized by the dimensionless variable:

$$\xi = \frac{s^2}{z} \quad (20)$$

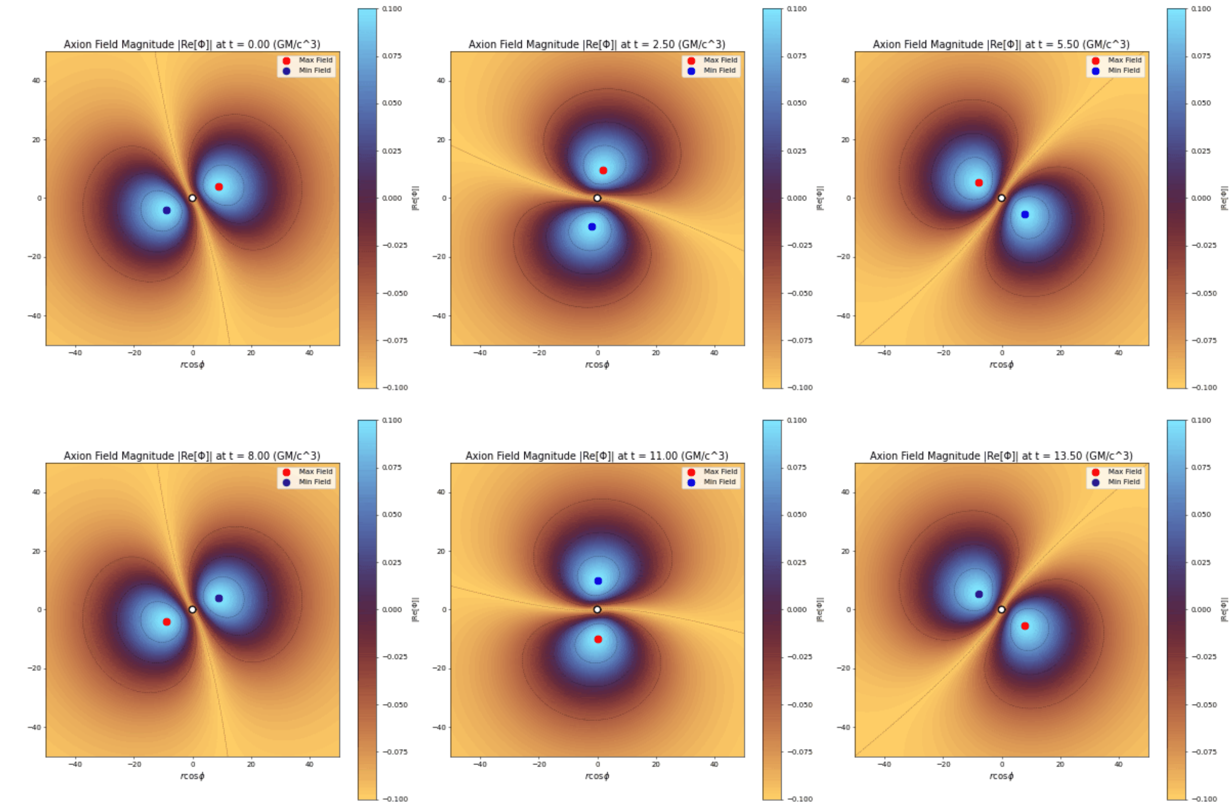

Figure 3: Polar evolution of axion cloud in n=2, l=m=1 state over time. Due to the quantum numbers, the axion field has a two-lobe shape, analogous to the p-orbitals of the hydrogen atom with the same quantum numbers. The cloud rotates counterclockwise.

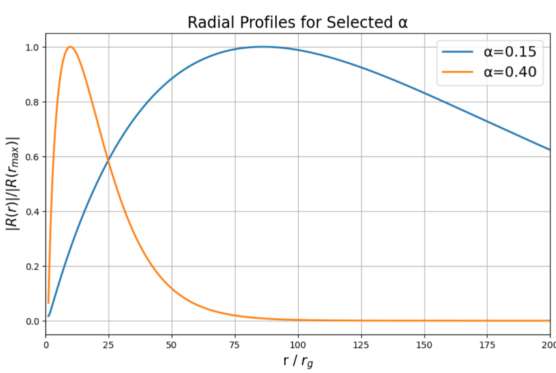

Figure 4: Radial profiles for axion cloud with fine structure constant values of 0.4 and 0.15.

This self-similarity allows the magnetic flux Φ, current I, and field-line angular velocity Ω_B to be expressed as functions of ξ alone, rather than s and z independently. The magnetic field components are then derived from the flux function through:

$$B_s = -\frac{1}{2\pi s}\frac{\partial \Phi}{\partial z}, \quad B_z = \frac{1}{2\pi s}\frac{\partial \Phi}{\partial s} \tag{21}$$

with the toroidal component given by:

$$B_\phi = \frac{I(\xi)}{2\pi s} \tag{22}$$

For a force-free plasma, where the Lorentz force vanishes ($\rho\mathbf{E} + \mathbf{j}\times\mathbf{B} = 0$), the current satisfies:

$$I(\xi) = -\frac{2\Omega_B}{\Phi'} \tag{23}$$

where primes denote derivatives with respect to ξ.

The specific functional forms for $\Phi(\xi)$ and $\Omega_B(\xi)$ are obtained by fitting to azimuthally averaged quantities from GRMHD simulations of a magnetically arrested disk around a spinning black hole (**?**). **?** adopt:

$$\Phi(\xi) = \tanh(0.3\xi) \tag{24}$$

$$\Omega_B(\xi) = 0.15\exp(-0.3\xi^2) \tag{25}$$

These fitting functions capture the essential structure of the jet: a highly magnetized spine near the axis (small ξ) surrounded by return currents at larger radii (larger ξ). The velocity field includes both poloidal components derived from the electromagnetic structure and a toroidal component from field-line rotation.

For application to M87, the model is scaled using a black hole mass of $M_{\mathrm{BH,M87}} = 6.6\times10^9\,M_\odot$, corresponding to a gravitational radius $r_g \approx 10^{13}$ m and light-crossing time ~ 9 hours. The magnetic flux is normalized to $\Phi_{z,\mathrm{M87}} \approx 10^{26}$ Wb, consistent with estimates for M87's jet. The viewing angle is set to $\theta = 20^\circ$, matching observational constraints for M87.

4.2. *Constant β_e Model for Plasma Emission*

To convert the electromagnetic structure into observable synchrotron emission, we require a prescription for the particle energy distribution. The model employs a "constant β_e" prescription, where the partial pressure $\tilde{P}_e$ of synchrotron-emitting relativistic electrons and positrons is related to the local magnetic pressure:

$$\tilde{P}_e = \beta_{e0} P_B = \beta_{e0} \frac{B^2}{2} \tag{26}$$

Here β_{e0} is a dimensionless parameter representing the ratio of particle pressure to magnetic pressure. This formulation is motivated by the expectation that a fraction of the electromagnetic energy density is converted to particle energy through processes such as magnetic reconnection, shocks, or turbulent acceleration.

The subequipartition regime ($\beta_{e0} \ll 1$) is expected for the highly magnetized inner jet regions that dominate millimeter-wavelength emission. Based on observational constraints from M87's spectrum and jet geometry, characteristic values are $\beta_{e0} \sim 10^{-10}$ to 10^{-6}, with lower values corresponding to more magnetized plasmas closer to the black hole.

The emitting particles are assumed to follow a power-law energy distribution:

$$N_e(\gamma) = K_e \gamma^{-p} \quad \text{for } \gamma_{\min} < \gamma < \gamma_{\max} \tag{27}$$

where γ is the particle Lorentz factor, p is the spectral index (typically $p \approx 2.5$–3 for AGN jets), and $\gamma_{\min} = 10$ represents the minimum energy of relativistic particles contributing to synchrotron emission. This distribution captures the non-thermal particle acceleration processes operating in relativistic jets.

For plasmas containing a mixture of electrons, positrons, and protons/ions, the model can be generalized to account for composition. If we denote the ion number density as n_i and the total particle density as n, the effective emitting particle pressure becomes:

$$\tilde{P}_e = \frac{n - n_i}{n} \beta_{e0} P_B \tag{28}$$

This modification reflects the fact that only electrons and positrons contribute significantly to synchrotron emission at observed frequencies—protons are too massive (by a factor of 1836) to emit efficiently at the same energies.

4.3. *Polarized Radiative Transfer*

The polarized synchrotron emission is described using the Stokes parameters (I, Q, U, V), which fully characterize the intensity and polarization state of the radiation. The evolution of these parameters along a photon trajectory is governed by the polarized radiative transfer equation:

$$\frac{d}{ds}\begin{pmatrix} I \\ Q \\ U \\ V \end{pmatrix} = \begin{pmatrix} j_I \\ j_Q \\ j_U \\ j_V \end{pmatrix} - \begin{pmatrix} \alpha_I & \alpha_Q & \alpha_U & \alpha_V \\ \alpha_Q & \alpha_I & \rho_V & -\rho_U \\ \alpha_U & -\rho_V & \alpha_I & \rho_Q \\ \alpha_V & \rho_U & -\rho_Q & \alpha_I \end{pmatrix} \begin{pmatrix} I \\ Q \\ U \\ V \end{pmatrix} \tag{29}$$

where s is the affine parameter along the ray path. The source vector components j_I, j_Q, j_U, j_V represent polarized emission; $\alpha_I, \alpha_Q, \alpha_U, \alpha_V$ are absorption coefficients; and ρ_V, ρ_Q, ρ_U are Faraday rotation and conversion coefficients.

The emission and absorption coefficients are computed from the synchrotron formalism for a power-law particle distribution. These coefficients depend on the effective magnetic field $B_e = |\mathbf{B} \times \hat{n}|$, where $\hat{n}$ is the line-of-sight direction, and on the partial pressure $\tilde{P}_e$ through the β_{e0} parameter. The key dependencies are:

$$j_I \propto \beta_{e0} B_e^{(p+1)/2} \nu^{-(p-1)/2} \tag{30}$$

$$\alpha_I \propto \beta_{e0} B_e^{(p+2)/2} \nu^{-(p+4)/2} \tag{31}$$

with similar expressions for other Stokes components. The linear polarization components Q and U reflect the projected magnetic field orientation, while circular polarization V arises from higher-order effects and asymmetry in the particle distribution.

As polarized light propagates through magnetized plasma, Faraday rotation causes the plane of linear polarization to rotate:

$$\frac{d\chi}{ds} = \rho_V \tag{32}$$

where χ is the electric vector position angle (EVPA). The Faraday rotation coefficient is given by:

$$\rho_V \propto \frac{n_e B_\parallel}{\nu^2} \tag{33}$$

where $B_\parallel$ is the magnetic field component parallel to the line of sight and n_e is the electron density. Faraday conversion (characterized by ρ_Q and ρ_U) couples circular and linear polarization modes.

For the plasma compositions considered, both electrons and positrons contribute to Faraday rotation, but with opposite signs due to their opposite charges. In a pure electron-positron plasma, these contributions partially cancel, while in electron-proton plasmas, only electrons contribute significantly.

The radiative transfer equation is solved by integrating along rays from the observer plane (X, Y) backward through the jet to the far side. Special relativistic effects are incorporated through Doppler boosting factors that depend on the bulk fluid velocity and viewing angle. The observed frequency ν relates to the comoving frequency ν' through:

$$\nu = \mathcal{D}\nu', \quad \mathcal{D} = \frac{1}{\Gamma(1 - \vec{\beta} \cdot \hat{n})} \tag{34}$$

where Γ is the bulk Lorentz factor and $\vec{\beta}$ is the bulk velocity in units of c.

The model produces synthetic Stokes maps at observing frequencies of 86 GHz and 230 GHz—the two primary frequencies of Event Horizon Telescope observations. These maps reveal characteristic patterns: bilateral asymmetry in intensity I due to Doppler beaming, symmetric/antisymmetric structures in Q and U reflecting the helical magnetic field geometry, and varying degrees of circular polarization V depending on plasma composition and magnetization.

This framework provides the baseline polarized emission against which axion-induced modifications will be compared. As will be described in Section 5, the presence of an axion field introduces an additional contribution to the Faraday rotation coefficient, which alters the evolution of the Stokes parameters along photon trajectories and produces observable signatures in the polarization maps.

5. AXION ELECTRODYNAMICS AND RADIATIVE TRANSFER

Since the EHT can resolve electromagnetic signatures, including the polarized images of M87, we consider how these signatures would change in the presence of an axion field. While modified Maxwell equations help integrate the dynamics of axion-electromagnetic interactions, for generating ray traced images, it is more important to couple the the field to the radiative transfer equations to see how the photon polarization evolves as it propagates through an ALP field. Here, we use the geometric optics approximation of photons propagating through an ALP field in curved spacetime (Schwarz et al. 2021). The radiative transfer model is identical to (Chen et al. 2022) with main equations being pulled from it. This is then followed with our own radiative transfer model to align with the jet geometry.

5.1. *Modified Maxwell Equations*

When axions are coupled to electromagnetism, Maxwell's equations are modified in the presence of the field (Sikivie 1983). The modifications come from the interaction term in the Lagrangian.

$$\mathcal{L}_{a\gamma} = \frac{g_{a\gamma}}{4} a F_{\mu\nu}\tilde{F}^{\mu\nu} \tag{35}$$

The equations of motion for the axion and gauge fields can be written as,

$$\begin{aligned} \partial_t^2 a - \nabla^2 a + m_a^2\, a &= -\frac{g_{a\gamma}}{4}\, F_{\mu\nu}\tilde{F}^{\mu\nu} \\ \partial_\mu F^{\mu\nu} = -j^\nu, &\quad \partial_\mu \tilde{F}^{\mu\nu} = 0 \end{aligned} \tag{36}$$

where $j^\nu = g_{a\gamma}\partial_\mu \tilde{F}^{\mu\nu}$. From this, it is straightforward to derive the axion-modified Maxwell equations,

$$\nabla\cdot\mathbf{E} = \rho \;-\; g_{a\gamma}\mathbf{B}\cdot\nabla a \tag{37}$$

$$\nabla\times\mathbf{B} = \dot{\mathbf{E}} \;+\; \mathbf{J} \;+\; g_{a\gamma}\;\left(\,\dot{a}\,\mathbf{B} - \mathbf{E}\times\nabla a\,\right) \tag{38}$$

$$\nabla\times\mathbf{E} = -\dot{\mathbf{B}} \tag{39}$$

$$\nabla\cdot\mathbf{B} = 0 \tag{40}$$

Note, the axion-electromagnetic charge and current are defined as follows.

$$\rho_a = -\;g_{a\gamma}\mathbf{B}\cdot\nabla a, \quad \mathbf{J}_a = g_{a\gamma}\;\left(\,\dot{a}\,\mathbf{B} - \mathbf{E}\times\nabla a\,\right) \tag{41}$$

5.2. *Radiative Transfer*

For our radiative transfer analysis, we apply the geometric optics approximation. In the Lorenz gauge, the equation of motion for the electromagnetic field can be written,

$$\nabla_\mu\nabla^\mu A^\nu - R^\mu_\nu A_\mu = -g_{a\gamma\gamma}\left(\nabla_\mu a\right)\tilde{F}^{\mu\nu} \tag{42}$$

which under the geometric optics approximation has the following ansatz,

$$A_\mu(x) \sim \Re\big\{\,\bar{A}_\mu(x)\, e^{\,iS(x)/\varepsilon}\big\}. \tag{43}$$

Here, we define the four-dimensional wave vector as $k_\mu \equiv \frac{1}{\epsilon}\partial_\mu S(x)$. At leading order in ε^{-1}, photons follow null geodesics ($k^\mu k_\mu = 0$), and we require this condition to be true along the path of the photons. At next order, the vector potential expansion yields,

$$k^\mu\nabla_\mu\bar{A}^\nu + \frac{1}{2}\bar{A}^\nu\nabla_\mu k^\mu + g_{a\gamma\gamma}\epsilon^{\mu\nu\rho\sigma}\bar{A}_\sigma k_\rho\nabla_\mu a = 0. \tag{44}$$

This can be further simplified if we introduce a spacelike polarization vector ξ^μ that satisfies $\xi_\mu k^\mu = 0$. This allows us to decompose the vector potential equation into two equations, one for amplitude $\bar{A}$ and one for polarization vector.

$$k^\mu\nabla_\mu\bar{A} + \frac{1}{2}\bar{A}\nabla_\mu k^\mu = 0 \tag{45}$$

$$k^\mu\nabla_\mu\xi^\sigma + g_{a\gamma\gamma}\epsilon^{\mu\nu\rho\sigma}k_\mu\xi_\nu\nabla_\rho a = 0 \tag{46}$$

Note that the equation of motion for $\bar{A}$ does not contain the axion field. This means that the intensity of the light is not affected by the presence of the field. Projecting onto circular polarization states and the reference frame of the observer, one can show that the left- and right-handed modes acquire opposite phase shifts proportional to the change in the axion field along the ray. For a linearly polarized photon, this corresponds to a net rotation of the electric-vector position angle (EVPA)

$$\Delta\chi \;\approx\; g_{a\gamma}\left[a(\text{observer}) - a(\text{emission})\right], \tag{47}$$

It is usually best, and most convenient, to describe photon propagation near the BH with the covariant, polarized, radiative transfer equations, solving for the Stokes vector I = (I, Q, U, V). These include j_S, absorption α_S, as well as Faraday rotation/conversion coefficients ρ_V, ρ_Q, ρ_U. As stated before, the intensity of the light is unaffected. The axion field can alter the Faraday converseion coefficient term. Splitting contributions from the plasma and the axions we can define the projection matrix,

$$M = M_{\text{plasma}} + M_{\text{axion}} \tag{48}$$

where the first term is exactly the Muller Matrix in the ordinary radiative transfer equations,

$$M_{\text{plasma}} \equiv \begin{pmatrix} \alpha_I & \alpha_Q & \alpha_U & \alpha_V \\ \alpha_Q & \alpha_I & \rho_V & -\rho_U \\ \alpha_U & -\rho_V & \alpha_I & \rho_Q \\ \alpha_V & \rho_U & -\rho_Q & \alpha_I \end{pmatrix} \tag{3.24}$$

The axion matrix is simply characterized as ,

$$M_{\text{axion}} = \begin{pmatrix} 0 & 0 & 0 & 0 \\ 0 & 0 & -2g_{a\gamma\gamma}\frac{da}{ds} & 0 \\ 0 & 2g_{a\gamma\gamma}\frac{da}{ds} & 0 & 0 \\ 0 & 0 & 0 & 0 \end{pmatrix} \tag{49}$$

Hence we get the following correction to the Faraday rotation,

$$\rho_V' = \rho_{plasma} - 2g_{a\gamma}\frac{da}{ds} \tag{50}$$

where s is the affine parameter of the photon trajectory. The derivative $\frac{da}{ds}$, which can be written as $k^\mu \partial_\mu a$, can be interpreted as the change in the axion field as "seen" by the photon along its trajectory. This arises from the parallel transport of the polarization vector in the presence of the axion gradient(i.e. change in axion field along the photon's worldline). In other words, for ray-traced images, the axion effect can be included by a change to the Faraday rotation coefficient. This directly affects the EVPA since,

$$\chi \equiv \frac{1}{2}\arg(Q + iU). \tag{51}$$

We can see this better by looking at the modified radiative transfer equation in local tangent space.

$$\frac{d}{ds}\begin{pmatrix} I \\ Q \\ U \\ V \end{pmatrix} = \begin{pmatrix} j_I \\ j_Q \\ j_U \\ j_V \end{pmatrix} - \begin{pmatrix} \alpha_I & \alpha_Q & \alpha_U & \alpha_V \\ \alpha_Q & \alpha_I & \rho_V' & \rho_U \\ \alpha_U & -\rho_V' & \alpha_I & \rho_Q \\ \alpha_V & -\rho_U & -\rho_Q & \alpha_I \end{pmatrix}\begin{pmatrix} I \\ Q \\ U \\ V \end{pmatrix} \tag{52}$$

5.3. *Radiative Transfer Model*

The Ambient dark matter model is the easiest to implement due to the simplicity of its solution. For the mass range we are concerned with, the extension of the jet does not surpass the radius of the soliton core. Thus, the NFW profile is not applied to the amplitude and the spatial gradients of the axion field vanish.

$$\rho_{a\gamma} = 2g_{a\gamma}k^\mu\partial_\mu a = 2g_{a\gamma}k^t\frac{da}{dt} = 2g_{a\gamma}E_\gamma\frac{da}{dt} \tag{53}$$

The value of $\rho_{a\gamma}$ is lower for lower energy photons. Thus, since $E_\gamma \propto \nu$, we expect to see smaller angle changes for the 86GHz case.

The superradiance case is much more complex since not only do we have to deal with all spatial gradients, we must make the geometry consistent with the jet and the radial function can only be evaluated numerically. Recall, we have the observer plane (X,Y), which are the polarization axes. We can parametrize the coordinates in terms of the self-similarity variable ζ so that it becomes the affine parameter.

$$\zeta = \frac{s^2}{z} \to s = \sqrt{\zeta z} \tag{54}$$

.

We then rotate the jet frame by θ around the x'-axis to align with the observer frame (X,Y,Z).

$$x' = X \tag{55}$$
$$y' = Ycos(\theta) + Zsin(\theta) \tag{56}$$
$$z' = Zcos(\theta) - Ysin(\theta) \tag{57}$$
$$s = \sqrt{X^2 + (Ycos(\theta) + Zsin(\theta))^2} \tag{58}$$

With some more algebra, we derive the following parametrizations of the cylindrical coordinates in terms of the affine parameter.

$$s(\zeta) = \sqrt{X^2 + (\zeta sin(\theta) - Ycos(\theta))^2} \tag{59}$$
$$\phi(\zeta) = ArcTan(\frac{X}{\zeta sin(\theta) - Ycos(\theta)}) \tag{60}$$
$$z(\zeta) = \zeta cos(\theta) + Y \tag{61}$$

Thus, to get the spatial components of the four-momentum, we differentiate each of these with respect to the affine parameter.

$$k^z = \frac{dz}{d\zeta} = cos(\theta) \tag{62}$$

6. RESULTS AND ANALYSIS

The main analysis showed in this paper is that of adding the soliton core model to the semi-analytic jet model. We use Python to compute the correction to the Faraday rotation coefficients and store it as a data frame. The data frame is exported to Mathematica for the semi-analytic computation of the relativistic jet's emission model, and solving the radiative transfer equations. Separate notebooks are used to study the 86GHz case and the 230GHz case, both frequencies the EHT can observe at. Two main cases are studied: maximal angle change for various masses and time oscillations. We restrict our analysis to use the coupling constant $g_{a\gamma} = 5.0 \times 10^{-17} GeV^{-1}$, simply to highlight how the maps are affected.

APPENDIX

A. WAVE DARK MATTER

B. BLANDFORD-ZNAJEK PROCESS

REFERENCES

Anantua, R., Emami, R., Loeb, A., & Chael, A. 2020, The Astrophysical Journal, 896, 30, doi: 10.3847/1538-4357/ab9103

Arvanitaki, A., & Dubovsky, S. 2011, Physical Review D, 83, doi: 10.1103/physrevd.83.044026

Arvanitaki, A., & Geraci, A. A. 2014, Phys. Rev. Lett., 113, 161801, doi: 10.1103/PhysRevLett.113.161801

Ayzenberg, D., Blackburn, L., Brito, R., et al. 2023, Fundamental Physics Opportunities with the Next-Generation Event Horizon Telescope. https://arxiv.org/abs/2312.02130

Baryakhtar, M., Galanis, M., Lasenby, R., & Simon, O. 2021, Physical Review D, 103, doi: 10.1103/physrevd.103.095019

Brito, R., Cardoso, V., & Pani, P. 2020, Superradiance: New Frontiers in Black Hole Physics (Springer International Publishing), doi: 10.1007/978-3-030-46622-0

Chen, Y., Li, C., Mizuno, Y., et al. 2022, Journal of Cosmology and Astroparticle Physics, 2022, 073, doi: 10.1088/1475-7516/2022/09/073

Chen, Y., Shu, J., Xue, X., Yuan, Q., & Zhao, Y. 2020, Phys. Rev. Lett., 124, 061102, doi: 10.1103/PhysRevLett.124.061102

Collaboration, T. E. H. T., Akiyama, K., Algaba, J. C., et al. 2021, The Astrophysical Journal Letters, 910, L12, doi: 10.3847/2041-8213/abe71d

Dolan, S. R. 2007, Phys. Rev. D, 76, 084001, doi: 10.1103/PhysRevD.76.084001

Event Horizon Telescope Collaboration, Akiyama, K., Alberdi, A., et al. 2019, ApJL, 875, L1, doi: 10.3847/2041-8213/ab0ec7

—. 2022, ApJL, 930, L12, doi: 10.3847/2041-8213/ac6674

—. 2024, ApJL, 964, L26, doi: 10.3847/2041-8213/ad2df1

Gorghetto, M., Hardy, E., & Nicolaescu, H. 2021, Journal of Cosmology and Astroparticle Physics, 2021, 034, doi: 10.1088/1475-7516/2021/06/034

Hui, L. 2021, Annual Review of Astronomy and Astrophysics, 59, 247–289, doi: 10.1146/annurev-astro-120920-010024

Lasota, J.-P., Gourgoulhon, E., Abramowicz, M., Tchekhovskoy, A., & Narayan, R. 2014, Physical Review D, 89, doi: 10.1103/physrevd.89.024041

Manita, Y., Takahashi, T., & Taruya, A. 2024, Soliton self-gravity and core-halo relation in fuzzy dark matter halos. https://arxiv.org/abs/2411.14614

Mina, M., Mota, D. F., & Winther, H. A. 2022, Astronomy amp; Astrophysics, 662, A29, doi: 10.1051/0004-6361/202038876

Mocz, P., Fialkov, A., Vogelsberger, M., et al. 2023, Monthly Notices of the Royal Astronomical Society, 521, 2608–2615, doi: 10.1093/mnras/stad694

Murphy, J. D., Gebhardt, K., & Adams, J. J. 2011, The Astrophysical Journal, 729, 129, doi: 10.1088/0004-637x/729/2/129

Noordhuis, D., Prabhu, A., Weniger, C., & Witte, S. J. 2024, Axion Clouds around Neutron Stars. https://arxiv.org/abs/2307.11811

Penrose, R., & Floyd, R. M. 1971, Nature, 229, 177. https://api.semanticscholar.org/CorpusID:121664446

Schive, H.-Y., Chiueh, T., & Broadhurst, T. 2014, Nature Physics, 10, 496–499, doi: 10.1038/nphys2996

Schwarz, D. J., Goswami, J., & Basu, A. 2021, Physical Review D, 103, doi: 10.1103/physrevd.103.l081306

Sikivie, P. 1983, Phys. Rev. Lett., 51, 1415, doi: 10.1103/PhysRevLett.51.1415

Teukolsky, S. A. 1972, Phys. Rev. Lett., 29, 1114, doi: 10.1103/PhysRevLett.29.1114

Tobar, M. E., McAllister, B. T., & Goryachev, M. 2019, Physics of the Dark Universe, 26, 100339, doi: 10.1016/j.dark.2019.100339

Weinberg, S. 1978, Phys. Rev. Lett., 40, 223, doi: 10.1103/PhysRevLett.40.223